# IMPROVED CONTRAST IN ULTRA-LOW-FIELD MRI WITH TIME-DEPENDENT BIPOLAR PREPOLARIZING FIELDS: THEORY AND NMR DEMONSTRATIONS

**Jaakko O. Nieminen[1], Jens Voigt[2], Stefan Hartwig[2], Hans Jürgen Scheer[2], Martin Burghoff[2], Lutz Trahms[2], Risto J. Ilmoniemi[1]**

1) Department of Biomedical Engineering and Computational Science, Aalto University School of Science, P.O. Box 12200, FI-00076 AALTO, Finland (✉ jaakko.nieminen@aalto.fi, +358 50 344 3186, risto.ilmoniemi@aalto.fi)

2) Physikalisch-Technische Bundesanstalt, Abbestr. 2–12, 10587 Berlin, Germany (jens.voigt@ptb.de, stefan.hartwig@ptb.de, hans-juergen.scheer@ptb.de, martin.burghoff@ptb.de, lutz.trahms@ptb.de)

**Abstract**

The spin–lattice ($T_1$) relaxation rates of materials depend on the strength of the external magnetic field in which the relaxation occurs. This $T_1$ dispersion has been suggested to offer a means to discriminate between healthy and cancerous tissue by performing magnetic resonance imaging (MRI) at low magnetic fields. In prepolarized ultra-low-field (ULF) MRI, spin precession is detected in fields of the order of 10–100 µT. To increase the signal strength, the sample is first magnetized with a relatively strong polarizing field. Typically, the polarizing field is kept constant during the polarization period. However, in ULF MRI, the polarizing–field strength can be easily varied to produce a desired time course. This paper describes how a novel variation of the polarizing–field strength and duration can optimize the contrast between two types of tissue having different $T_1$ relaxation dispersions. In addition, NMR experiments showing that the principle works in practice are presented. The described procedure may become a key component for a promising new approach of MRI at ultra-low fields.

Keywords: $T_1$ dispersion, prepolarization, polarizing field, ultra-low-field MRI.

## 1. Introduction

In conventional high-field magnetic resonance imaging (MRI), *i.e.*, in static fields of B > 1 T, the $T_1$ contrast between healthy and cancerous tissue is often modest, so that the discrimination of these tissue types is difficult without contrast agents [1]; on the other hand, $T_2$-weighted imaging without contrast agents has applications, *e.g.*, in the imaging of rectal cancer [2]. The discrimination using $T_1$ contrast may be easier at ultra-low fields (ULF) in the microtesla range: Recently it was shown that biopsies of prostate-cancer tissue have significantly shorter $T_1$ relaxation times than healthy prostate tissue in fields well below one millitesla [3]. Apparently, $T_1$ relaxation times of these tissue samples exhibit a dispersion that changes significantly towards lower Larmor frequencies, a behavior that facilitates the observation of contrast by ULF MRI. Other proposed applications of ULF MRI include detection of liquid explosives [4], hybrid magnetoencephalography-MRI [5,6], and direct imaging of neuronal currents [7,8]. The polarization method introduced in this paper is a technique that future optimized ULF-MRI scanners may benefit from.

This paper shows how $T_1$ dispersion contrast can be maximized by making use of a distinctive feature of the ULF-NMR measurement technique. In ULF NMR/MRI, the magnetization of the sample is usually prepared by a polarizing field in the range of a few millitesla. A field of this strength can easily be varied, unlike in conventional MRI where the fields in the tesla range are usually generated by superconducting magnets and only a limited variation of the field strength is possible. In the following, we describe how a novel variation

of the polarizing-field strength and duration can optimize the contrast between two types of tissue having different $T_1$ relaxation times and completely null the signal from a given tissue. In addition, we present NMR experiments which show that the principle works in practice.

## 2. Materials and methods

### 2.1. Method background

In conventional high-field MRI, $T_1$ weighting is commonly achieved by the inversion-recovery sequence [9,10]. A modification of this sequence has been used also for prepolarized MRI in the Earth's magnetic field [11]. In Ref. [12], Lee et al. further generalized this approach. On the other hand, injection of contrast agents that exhibit $T_1$ dispersions has also been demonstrated to be suitable to enhance image contrast in prepolarized [13] or fast field-cycling MRI [14]. Also nitrogen dips, which occur in the $T_1$ dispersion curves of tissues containing protein, have been demonstrated to offer means to improve image contrast in prepolarized MRI [15].

In the following, we describe in a general way how the sample magnetization generated by a time-dependent polarizing field can be calculated, provided the $T_1$ dispersion of the substance or tissue type is known. We also describe how the polarizing-field time course can be optimized to produce images with maximized contrast.

When exposed to a time-dependent magnetic field, the time dependence of the nuclear magnetization $M(t)$ of a sample follows the modified Bloch equation [16]. In a locally unidirectional field $B(t)$ and $M(t)$, this equation reads

$$\frac{dM}{dt} + \frac{M(t) - \alpha B(t)}{T_1(B(t))} = 0 \ , \tag{1}$$

where $\alpha$ is a constant describing the nuclear magnetic susceptibility and $T_1(B(t))$ is the field-strength-dependent longitudinal relaxation time. In general, $\alpha$ is also a function of $B$. However, at low fields, the field dependency of the susceptibility of diamagnetic tissues is small and can be neglected. With the initial condition $M(0) = 0$, the solution of (1) is

$$M(t) = \alpha \int_0^t \frac{B(\tau)}{T_1(B(\tau))} \exp\left[\int_t^\tau T_1^{-1}(B(s))ds\right]d\tau \ . \tag{2}$$

Equation (2) shows that the magnetization depends on $B(t)$ both directly and also via the $T_1$ relaxation time. In prepolarized MRI, the image intensity depends on the magnetization at the end of the polarization period.

Our aim is to find a polarizing-field time course that, at the end of the polarization period, maximizes the magnetization difference between two substances having different $T_1$ dispersions. Such a waveform would allow us to acquire high-contrast images. Generally, the $T_1(B)$ dispersion is tissue-specific. We want to find $B(t)$ that maximizes the difference:

$$\left|M_a(T) - M_b(T)\right| \ , \tag{3}$$

where $T$ is the polarization period and the subscripts refer to the two substances a and b with their specific $T_1$ dispersions. Because ULF MRI is robust against susceptibility variations [17], real-valued reconstruction is much easier than in high-field MRI, where tailored reconstruction algorithms are needed to correct the image phase [18,19]; thus, we can allow $M_a(T)$ and $M_b(T)$ to have opposite signs in (3) resulting in a contrast superior to magnitude images. Equally, we can also optimize the contrast-to-noise ratio CNR, which between substances a and b that have equal noise levels is defined as the difference between their signal-to-noise ratios (SNR): $CNR = |SNR_a - SNR_b|$. For example, with a prepolarized spin-echo sequence and a fixed total imaging time, we have for the substance a:

$$\text{SNR}_a \propto M_a(T)\exp\left(-\frac{T_E}{T_{2,a}}\right)\sqrt{\frac{T_E}{T + 3T_E/2}} \ , \tag{4}$$

where $T_E$ is the echo time, $T_{2,a}$ is the spin–spin relaxation time, and the factor under the square root is the fraction of the total imaging time that is available for data acquisition.

In practice, the maximum field strength $B_{max}$ is limited; thus, we have to obey the condition

$$|B| \le B_{max} \ . \tag{5}$$

One could also add other constraints like $|M_a(T)| \ge M_{min}$ or $|M_b(T)| \le M_{max}$ to guide the signal strengths to desired values. When the $T_1(B)$ dispersions are known, we can find the optimal $B(t)$ numerically. We require that $B(t)$ lies in a subspace spanned by piecewise-constant boxcar functions $\Pi_{t_{i-1},t_i}(t)$, which are 1 when $t_{i-1} < t \le t_i$ and zero otherwise:

$$B(t) = \sum_{i=1}^{n} B_i \Pi_{t_{i-1},t_i}(t) \ . \tag{6}$$

Now, we search for the optimal coefficients $B_i$ and parameters $t_i$, $i = 1, \ldots, n$. These field parameters are illustrated in Fig. 1. We define $0 = t_0 < t_1 < \ldots < t_n = T$. A combination of (2) and (6) gives

$$M(T) = \alpha \sum_{i=1}^{n} B_i \left[1 - \exp\left(-\frac{t_i - t_{i-1}}{T_1(B_i)}\right)\right] \exp\left(-\sum_{j=i+1}^{n} \frac{t_j - t_{j-1}}{T_1(B_j)}\right) \ . \tag{7}$$

Now, we have turned the nested integrations into simple summations; thus, we can efficiently maximize (3), as well as solve other similar optimization tasks. Generally, also other basis functions could be used making the polarizing-field time course, *e.g.*, smooth; however, they tend to increase the computational cost of the optimization, as the integrals in (2) have to be carried out numerically. If needed, the formalism can be easily generalized to allow such basis functions.
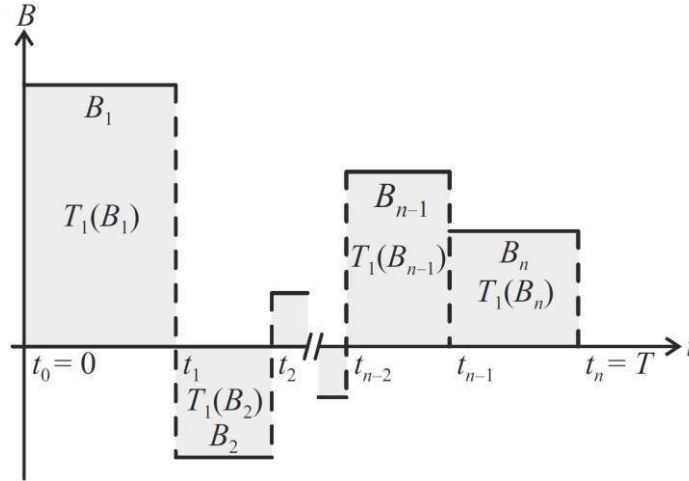
Fig. 1. A schematic diagram of a polarizing field illustrating the notation used in the text.

To find the optimized time course for the polarizing field, we first have to measure the $T_1$-dispersion data for the two substances within the available polarizing-field strengths. To the measured dependence of $1/T_1$ over $B$, we can fit Cole–Cole expression curves:

$$\frac{1}{T_1(B)} = A \, \mathrm{Re}\left[\frac{1}{1 + (iB/B_c)^{\beta/2}}\right] + C \, , \tag{8}$$

where $A$, $B_c$, $\beta$, and $C$ are fitting parameters and $i = \sqrt{-1}$ [20]. Using these fits, we can interpolate $T_1$ values also for those field amplitudes that we did not measure and reduce the effect of noise in the $T_1$ estimates. With the dispersion information and (7) at hand, we can implement an optimization algorithm to find the optimal time course for the polarizing field maximizing (3).

We optimized the polarizing-field time courses with Mathematica (Wolfram Research, Inc., Champaign, IL, USA) using its simulated-annealing algorithm and by increasing the number of optimization parameters gradually. First, we had three optimization parameters in the task, *i.e.*, two amplitudes ($B_1$ and $B_2$) for the polarizing field and one time parameter ($t_1$) indicating the time when the field amplitude changes. We optimized the polarizing field with these parameters subject to the constraints $|B_1|, |B_2| \leq B_{max}$, $0 < t_1 < T$, and $M_b(T) = 0$. Next, we increased the number of field steps by one resulting in five parameters ($B_1$, $B_2$, $B_3$, $t_1$, and $t_2$). Then, we searched for the optimal field again. We increased the number of field steps and repeated the optimization until we found no significant improvements in the value of (3).

In order to demonstrate that the introduced procedure would also improve CNR given a fixed total imaging time, which could include signal averaging, we performed simulations in the following setting. We optimized the waveform of the polarizing field to maximize the SNR difference between two agarose-gel solutions, as given by (4), subject to the constraint that the other sample would produce no signal. For this, we assumed that the image formation would occur at a field of 50 μT and that at that field $T_2 = T_1$. The optimization was done in a similar incremental manner as above, except that now also the values of $T$ and $T_E$ were optimized.

The results with the optimized waveforms were compared to those that can be achieved with the conventional inversion-recovery sequence. For this purpose, we considered a polarizing sequence having first the field $B$ on for time $T_{inv}$. After this, the field was inverted

to $-B$, which was on for time $T-T_{inv}$. When maximizing (3) for a fixed $T$, we optimized the values of $B$ and $T_{inv}$. For CNR maximization, we optimized also the parameters $T$ and $T_E$. In both cases, we used the same constraints as in the optimization of the general polarizing-field time courses.

### 2.2. Experimental implementation

In order to validate the concept of our approach by measurements on test samples, we produced two agarose-gel solutions containing 0.25 and 0.50 mass-% of agarose gel, respectively. Agarose gel is known to exhibit a field dependency of the $T_1$ dispersion in the range between 0.1 and 10 mT, which scales with the agarose concentration [12]. Here, we use the different longitudinal $T_1$ relaxation times and the strong changes of both samples around 1 mT as a testbed for our method.

To this end, we first had to measure the $T_1$ dispersions to have input data for the calculations according to (7). The measurements were performed using the SQUID (superconducting quantum interference device) system described in Ref. [21]. Polarizing and detection fields were generated by two Helmholtz coils oriented perpendicular to each other. The $T_1$ relaxation times were determined by two different methods. In the range of 1 µT–1 mT, the method of Ref. [12] was used: First, the nuclear magnetization was produced by a polarizing field of 4.8 mT. After 2 s, the polarizing field was reduced quickly to an evolution field $B_e$. In $B_e$, the sample magnetization relaxed during time $t_e$ according to $T_1(B_e)$. To observe the decreased magnetization, $B_e$ was switched off after time $t_e$, and a perpendicular detection field of 9 µT was applied. Due to the change of field direction, a free precession decay (FPD) was initiated. The FPD signal was detected by the SQUID system. The initial amplitude of the measured FPD was estimated by fitting an exponential function to the data [22]. Finally, the estimated amplitude was used to determine the $T_1$ relaxation rate in $B_e$.

To measure $T_1$ in fields above 1 mT, a method previously described in Ref. [21] was applied. The method utilizes the increase of the sample magnetization with the duration of a polarizing field. To measure the increasing magnetization, the polarizing field was switched off and the sample magnetization was let to precess about a perpendicular and permanently present detection field of 9 µT. To estimate one $T_1$ value, regardless of which one of the two methods was used, we measured 8 FPDs with different field durations.

### 3. Results

Fig. 2 shows the measured $T_1$ relaxation values of the agarose gel solutions over the field range 1.2 µT–4.8 mT. As expected from Ref. [12], the data reveal that the $T_1$ values change rapidly when the field is varied from 1 to 4.8 mT. The $T_1$ relaxation rate increases roughly proportionally to the agarose content, so that the dispersion curves of the two samples differ by a factor of two but exhibit similar shapes. To the measured dependence of $1/T_1$ over $B$, we fitted Cole–Cole expression curves, (8), which are also shown in Fig. 2; the obtained parameters and their standard errors are listed in Table 1. The Cole–Cole fits of the two agarose concentrations were used as input data for calculating the magnetization generated by the temporal sequence of the polarizing fields. We designed the polarizing fields using the above-described optimization procedure for 2.5-s-long polarizing fields. To cope with our experimental conditions, we limited the amplitude of the polarizing field to be below $B_{max} = 4.8$ mT. We found optimized solutions in terms of (3) and (5), where one of the samples exhibited zero magnetization while the other had maximum amplitude.
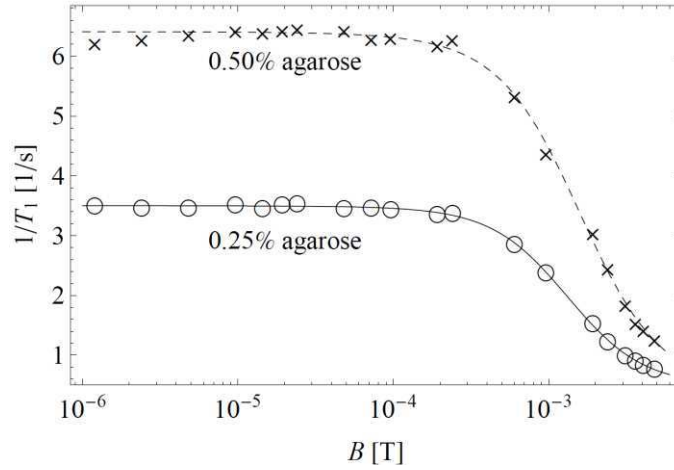
Fig. 2. Measured $T_1$ relaxation values for the 0.25% and 0.50% agarose gel samples for field values 1.2 µT–4.8 mT. These data are basically a replica of measurements in Ref. [12]. Also shown are the fitted Cole–Cole expression curves, which were used for subsequent waveform optimizations.

Table 1. Parameter estimates and their standard errors for the fitted Cole–Cole expression curves.

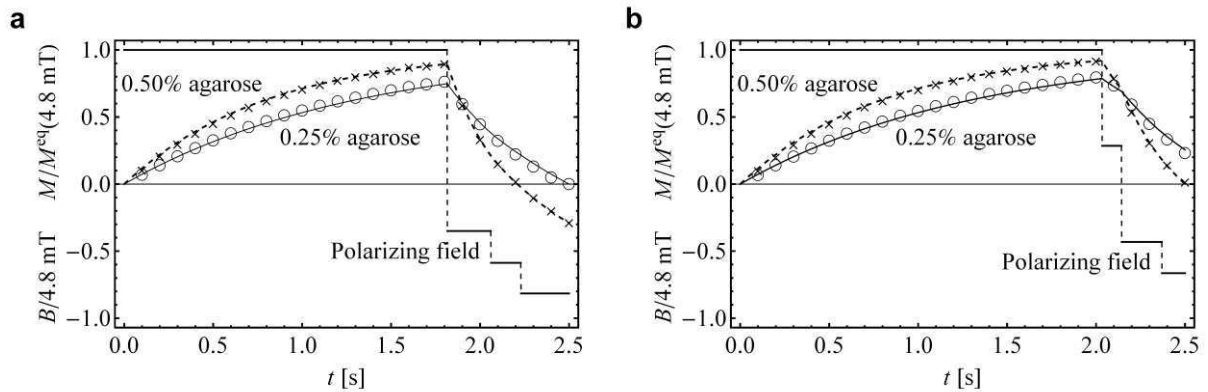|  | 0.25% agarose | 0.50% agarose |
|---|---|---|
| $A$ [1/s] | $3.04 \pm 0.06$ | $6.0 \pm 0.3$ |
| $B_c$ [mT] | $1.32 \pm 0.04$ | $1.6 \pm 0.1$ |
| $\beta$ | $1.89 \pm 0.03$ | $1.84 \pm 0.05$ |
| $C$ [1/s] | $0.46 \pm 0.05$ | $0.4 \pm 0.2$ |



Fig. 3. Experimental results showing how the magnetizations of the 0.25% and 0.50% agarose samples develop in optimized time-dependent polarizing fields. In (a), the 2.5-s-long polarizing waveform was designed to maximize the magnetization of the 0.50% agarose sample while producing zero magnetization for the 0.25% agarose sample. In (b), the 2.5-s-long polarizing waveform aimed at maximizing the magnetization of the 0.25% agarose sample while producing zero magnetization for the 0.50% agarose sample. The magnetization values are normalized with the equilibrium magnetizations, $M^{eq}$, at 4.8 mT. Also shown are the curves representing the theoretical evolution of the magnetizations and the polarizing waveforms.

In Fig. 3a, we show a 2.5-s-long polarization sequence designed to maximize the magnetization of the 0.50% agarose gel sample while producing zero magnetization for the 0.25% agarose sample. The polarizing field has four discrete steps; the final magnetization of the 0.50% agarose gel sample did not seem to increase when we increased the number of field

steps above four. Fig. 3b shows a waveform that maximizes the magnetization of the 0.25% agarose gel sample while producing zero magnetization for the 0.50% agarose sample. Also in this case, we found no improvements when we increased the number of field steps above four.

We validated these solutions experimentally by implementing the optimized polarizing-field sequence in our measurement set–up. In order to measure the evolution of the magnetization of the two agarose samples as a function of time, we interrupted the sequence at some time instant and followed up the detection procedure described above. This procedure was repeatedly applied for various evolution times, which were increased stepwise by 100 ms until the entire interval of 2.5 s was covered.

In Fig. 3, the experimental data acquired in this way are shown illustrating how the magnetizations of the two samples evolve during the polarization. Notably, the measured data points closely follow the curves predicted by the calculations indicating that the transitions between consecutive polarizing-field amplitudes are fast enough. Note also that when maximizing the signal from the 0.25% agarose sample, the final magnetization remains positive, because its $T_1$ values are greater than those of the 0.50% agarose sample. In contrast, when we maximized the signal from the 0.50% the faster relaxation processes produce a zero crossing to the evolution curve.

For comparison, we also calculated the polarization behavior of the two samples for inversion-recovery sequences utilizing inversion of the polarizing field, again obeying the limiting condition of $B_{max} = 4.8$ mT. Optimal inversion-recovery sequences with duration $T = 2.5$ s, which maximize the signal of the 0.25% and 0.50% agarose samples, respectively, while leaving the other magnetization at zero, were obtained with inversion times of 1.98 s and 1.77 s, respectively, with $B = B_{max}$. In comparison to these data, the polarizations in Fig. 3a and b are 23% and 31% higher, respectively. With other substances having different $T_1$ dispersions and with different optimization goals, we expect even larger differences between optimized time-dependent polarizing fields and the inversion-recovery sequence.

Optimal sequences to maximize CNR between the two agarose-gel solutions, with $B_{max} = 4.8$ mT, are illustrated in Fig. 4. These sequences start with a time-dependent polarization period, which guarantees that the signal from one of the agarose-gel solutions is zero. Subsequently, imaging in a field of 50 μT follows. The polarization periods for maximizing the SNR of the 0.25% and 0.50% agarose samples were $T = 3.11$ s and $T = 2.72$ s, respectively. The respective echo times were $T_E = 134$ ms and $T_E = 75$ ms. For comparison, we found that when maximizing the SNR of the 0.25% agarose sample, the optimal inversion-recovery sequences would have $T_E = 136$ ms, $T = 3.86$ s, and $T_{inv} = 3.30$ s. When maximizing the SNR of the 0.50% agarose solution, the respective values are $T_E = 76$ ms, $T = 3.58$ s, $T_{inv} = 2.76$ s. In both cases, $B = B_{max}$. However, the optimized polarizing-field time courses outperform the inversion-recovery sequence also in this case: The CNR produced by the sequences depicted in Fig. 4a and b are 18% and 22% higher than the respective values for the optimized inversion-recovery sequences.
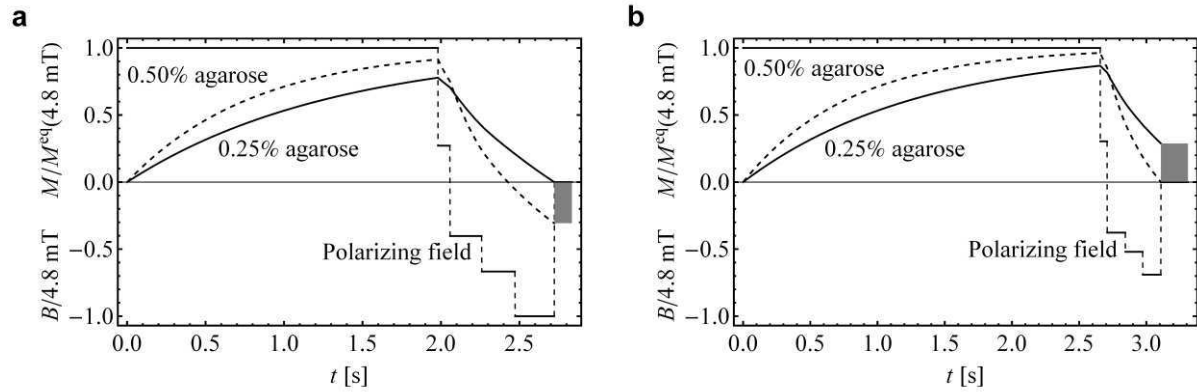
Fig. 4. Simulation results showing sequences for maximizing image CNR per unit time. In (a), the polarizing waveform and the echo time were designed to maximize the SNR of the 0.50% agarose-gel solution while producing zero signal for the 0.25% agarose-gel solution. In (b), the polarizing waveform maximizes the SNR of the 0.25% agarose sample while producing zero signal for the 0.50% agarose sample. The magnetization values are normalized with the equilibrium magnetizations, $M^{eq}$, at 4.8 mT. The gray rectangles represent signal acquisition in a field of 50 μT spanning the time $3T_E/2$.

## 4. Discussion

The excellent congruence between theoretical predictions and experimentally realized time-dependent magnetization indicates that the suggested method will work in reality to create contrast between samples with different $T_1$ dispersions. A prerequisite of the method is the knowledge of the $T_1(B)$ dependencies over the available polarizing-field strengths. This means that in a real situation, where the task is to generate high-contrast magnetic resonance images, one has to measure the $T_1(B)$ dispersion of the tissue types of interest in advance. However, much of this work has already been done, as the relaxation dispersion has been studied extensively within a wide range of field values (~200 μT–2 T) both for healthy [20,23,24] and pathological tissue [25]. Note also that the image contrast can be optimized also based on partial or slightly inaccurate dispersion information. Although we focused on $T_1$ dispersion, the contrast optimization could equally well be formulated using $T_2$ dispersion. However, because the transverse relaxation is affected by instrumentation-specific field inhomogeneities, we think that $T_1$ dispersion is better suited for contrast optimization.

For the shown example of two agarose samples with different $T_1(B)$, we could improve the contrast of prepolarized ULF MRI significantly compared to an optimized conventional inversion recovery. The situation may be even more favorable if the dispersion changes of the two samples do not occur in the same field range as was the case in our study. Note, however, that dispersion changes are not a mandatory prerequisite for this approach; it is sufficient that the $T_1$ values are different.

The presented concept, based on bipolar polarizing fields, could also be realized by applying unipolar polarizing fields and utilizing π pulses to flip the magnetization direction whenever the field direction should change. However, then either the frequencies of the π pulses should vary according to the polarizing field or the pulses should be applied together with a short-duration field of a fixed strength. In this study, we limited the formalism for two substances. However, the approach can be generalized to include more $T_1$ curves, as long as the optimization task can be formulated mathematically. Naturally, constraints restricting the polarizing field to be purely positive may also be included in the optimization.

Although the developed formalism is general, we presented results subject to the constraint that one of the studied substances produced no signal. We think the use of this constraint is

useful also in practice, as otherwise partial-volume effects on tissue boundaries may introduce ambiguity on how to define the extent of the studied tissues in the images.

In conclusion, we have presented a procedure by which $T_1$ contrast in ULF-MR images can be optimized. It is made possible by the special feature of ULF NMR that the nuclear magnetization can easily be manipulated by an appropriate design of the polarizing-field sequence. This procedure may become a key method for the promising new approach of MRI at very low fields. In particular, time-dependent polarizing fields could significantly improve the performance of ULF MRI as a tool for the imaging of cancerous tissues without contrast agents.

## Acknowledgements

## References

[1] Strijkers G.J., Mulder W.J.M., van Tilborg G.A.F., Nicolay K. (2007). MRI contrast agents: current status and future perspectives. *Anti-Cancer Agents Med. Chem.*, 7(3), 291-305.

[2] Klessen C., Rogalla, P., Taupitz M. (2007). Local staging of rectal cancer: the current role of MRI. *Eur. Radiol.*, 17(2), 379-389.

[3] Busch S., Hatridge M., Mößle, Myers W., Wong T., Mück M., Chew K., Kuchinsky K., Simko J., Clarke J. (2012). Measurements of $T_1$-relaxation in ex vivo prostate tissue at 132 μT. *Magn. Reson. Med.*, 67(4), 1138-1145.

[4] Espy M., Flynn M., Gomez J., Hanson C., Kraus R., Magnelind P., Maskaly K., Matlashov A., Newman S., Owens T., Peters M., Sandin H., Savukov I., Schultz L., Urbaitis A., Volegov P., Zotev V. (2010). Ultra-low field MRI for the detection of liquid explosives. *Supercond. Sci. Technol.*, 23(3), 034023.

[5] Zotev V.S., Matlashov A.N., Volegov P.L., Savukov I.M., Espy M.A., Mosher J.C., Gomez J.J., Kraus Jr., R.H. (2008). Microtesla MRI of the human brain combined with MEG. *J. Magn. Reson.*, 194(1), 115-120.

[6] Vesanen P.T., Nieminen J.O., Zevenhoven K.C.J., Dabek J., Parkkonen L.T., Zhdanov A.V., Luomahaara J., Hassel J., Penttilä J., Simola J., Ahonen,A.I., Mäkelä J.P., Ilmoniemi R.J. (2013). Hybrid ultra-low-field MRI and MEG system based on a commercial whole-head neuromagnetometer, *Magn. Reson. Med.* 69(6), 1795-1804.

[7] Kraus Jr., R.H., Espy M.A., Volegov P.L., Matlachov A.N., Mosher J.C., Urbaitis A.V., Zotev V.S. (2007). Toward SQUID-based direct measurement of neural currents by nuclear magnetic resonance. *IEEE Trans. Appl. Supercond.*, 17(2), 854-857.

[8] Burghoff M., Albrecht H.H., Hartwig S., Hilschenz I., Körber R., Höfner N., Scheer H.-J., Voigt J., Trahms L., Curio G. (2010). On the feasibility of neurocurrent imaging by low-field nuclear magnetic resonance. *Appl. Phys. Lett.*, 96(23), 233701.

[9] Bydder G.M., Young I.R. (1985). MR imaging: Clinical use of the inversion recovery sequence. *J. Comput. Assist. Tomogr.*, 9(4), 659-675.

[10] Bydder G.M., Steiner R.E., Blumgart L.H., Khenia S., Young I.R. (1985). MR imaging of the liver using short TI inversion recovery, *J. Comput. Assist. Tomogr.*, 9(6), 1084-1089.

[11] Planinšič G., Stepišnik J., Kos M. (1994). Relaxation-time measurement and imaging in the Earth's magnetic field. *J. Magn. Reson. A*, 110(2), 170-174.

[12] Lee S.K., Mößle M., Myers W., Kelso N., Trabesinger A., Pines A., Clarke J. (2005). SQUID-detected MRI at 132 μT with $T_1$-weighted contrast established at 10 μT–300 mT. *Magn. Reson. Med.*, 53(1), 9–14.

[13] Alford J.K., Rutt B.K., Scholl T.J., Handler W.B., Chronik B.A. (2009). Delta relaxation enhanced MR: Improving activation-specificity of molecular probes through $R_1$ dispersion imaging. *Magn. Reson. Med.*, 61(4), 796-802.

[14] Hógáin D.Ó., Davies G.R., Baroni S., Aime S., Lurie D.J. (2011). The use of contrast agents with fast field-cycling magnetic resonance imaging. *Phys. Med. Biol.*, 56(1), 105-115.

[15] Ungersma S.E., Matter N.I., Hardy J.W., Venook R.D., Macovski A., Conolly S.M., Scott G.C. (2006). Magnetic resonance imaging with $T_1$ dispersion contrast. *Magn. Reson. Med.*, 55(6), 1362-1371.

[16] Abragam A. (1961). *The Principles of Nuclear Magnetism*. Oxford: Clarendon Press. p. 53.

[17] Tseng C.H., Wong G.P., Pomoroy V.R., Mair R.W., Hinton D.P., Hoffmann D., Stoner R.E., Hersman F.W., Cory D.G., Walsworth R.L. (1998). Low-field MRI of laser polarized noble gas. *Phys. Rev. Lett.*, 81(17), 3785-3788.

[18] Park H.W., Cho M.H., Cho Z.H. (1986). Real-value representation in inversion-recovery NMR imaging by use of a phase-correction method. *Magn . Reson. Med.*, 3(1), 15-23.

[19] Xiang Q.S. (1996). Inversion recovery image reconstruction with multiseed region-growing spin reversal. *J. Magn. Reson. Imaging*, 6(5), 775-782.

[20] Koenig S.H., Brown R.D. (1987). III Relaxometry of tissue, In Grupta, R.K., editor. *NMR Spectroscopy of Cells and Organisms, Vol. II*, Boca Raton, FL: CRC Press. p. 75-114.

[21] Burghoff M., Hartwig S., Trahms L., Bernading J. (2005). Nuclear magnetic resonance in the nanoTesla range. *Appl. Phys. Lett.*, 87(5), 054103.

[22] Burghoff M., Albrecht H.H., Hartwig S., Hilschenz I., Körber R., Sander Thömmes T., Scheer H.J., Voigt J., Trahms L. (2009). SQUID system for MEG and low field magnetic resonance. *Metrol. Meas. Syst.* 16(3), 371-375.

[23] Bottomley P.A., Foster T.H., Argersinger R.E., Pfeifer L.M. (1984). A review of normal tissue hydrogen NMR relaxation times and relaxation mechanisms from 1–100 MHz: dependence on tissue type, NMR frequency, temperature, species, excision, and age. *Med. Phys.*, 11(4), 425-448.

[24] Fischer H.W., Rinck P.A., van Haverbecke Y., Muller R.N. (1990). Nuclear relaxation of human brain gray and white matter: analysis of field dependence and implications for MRI. *Magn. Reson. Med.*, 16(2), 317-334.

[25] Bottomley P.A., Hardy C.J., Argersinger R.E., Allen-Moore G. (1987). A review of ^{1}H nuclear magnetic resonance relaxation in pathology: Are $T_1$ and $T_2$ diagnostic? *Med. Phys.*, 14(1), 1-37.